

Direct numerical simulation of homogeneous turbulence with hyperviscosity

A. G. Lamorgese, D. A. Caughey, and S. B. Pope
*Sibley School of Mechanical and Aerospace Engineering, Cornell University, Ithaca,
 New York 14853-7501*

(Received 18 April 2004; accepted 15 October 2004; published online 15 December 2004)

We perform direct numerical simulations (DNS) of the hyperviscous Navier–Stokes equations in a periodic box. We consider values of the hyperviscosity index $h=1, 2, 8$, and vary the hyperviscosity to obtain the largest range of lengthscale ratios possible for well-resolved pseudo-spectral DNS. It is found that the spectral bump, or bottleneck, in the energy spectrum observed at the start of the dissipation range becomes more pronounced as the hyperviscosity index is increased. The calculated energy spectra are used to develop an empirical model for the dissipation range which accurately represents the bottleneck. This model is used to predict the approach of the turbulent kinetic energy k to its asymptotic value, k_∞ , as the hyperviscosity tends to zero. © 2005 American Institute of Physics. [DOI: 10.1063/1.1833415]

I. INTRODUCTION

Recent experimental measurements^{1–4} in homogeneous turbulence at high Reynolds numbers show the unequivocal presence of a “bottleneck” effect. This phenomenon is observed in longitudinal and transverse energy spectra alike. In the aforementioned works, data for the longitudinal energy spectrum $E_{11}(\kappa_1)$ (where κ_1 is the wave number) are shown to satisfy $-5/3$ -scaling in an inertial range of scales (corresponding to a “plateau” in the compensated spectra, see Figs. 1 and 2). At larger wave numbers ($\kappa_1 \eta \approx 0.05$), a bump-like (or bottleneck) behavior is observed, followed by the spectrum’s monotonic decay further in the dissipation range.

Similar bumps have been documented in pseudo-spectral direct numerical simulations (DNS) of homogeneous turbulence.^{5–7} Even in the absence of experimental data to compare with, such bumps may not be explained in terms of numerical discretization effects, as they are evident in pseudo-spectral DNS in which the numerical errors have been demonstrated to be small in comparison.^{7,8} In other words, bottleneck bumps as observed in DNS are (at least qualitatively) consistent with those observed in recent experiments.

Recent work on the hyperviscosity-modified Navier–Stokes equation⁹ (with hyperviscosity index h) has clarified the connection that this approach has with large-eddy simulation. We note, however, that it is unclear whether hyperviscous subgrid-scale models are capable of reproducing realistic features of internal intermittency in the inertial range. Relevance of the hyperviscous ($h > 1$) Navier–Stokes equation is not restricted to the large-eddy simulation of conventional ($h=1$) turbulence. Hyperviscous Navier–Stokes simulations may be a useful testbed for two-point closure theories (e.g., a hyperviscous variant of EDQNM).

In the more basic context of the Kolmogorov (1941) phenomenology, it is still unclear whether the hyperviscous Navier–Stokes equation (with $h > 1$) contains any physics of bottleneck effects that are evident in conventional ($h=1$) turbulence. It is plausible that a “parametrization” of bottleneck

effects in hyperviscous ($h > 1$) turbulence may shed light on bottleneck effects in conventional ($h=1$) turbulence.

In this work, our initial goal is the construction of a dataset of DNS of the normal ($h=1$) and hyperviscous ($h > 1$) Navier–Stokes equation. We use such data in the modeling of bottleneck effects in energy spectra in homogeneous, nondecaying turbulence. The result is a model spectrum that is capable of matching numerical spectra to good accuracy because of its ability to account for the bottleneck. Finally, we attempt to use the model spectrum to investigate the Reynolds number dependence of energy spectra as the Reynolds number grows unbounded.

II. HYPERVISCIOUS, FORCED DNS

In the following, $\mathbf{u}(\mathbf{x}, t)$ denotes the fluctuating component of a zero-mean solenoidal velocity field governed by the forced hyperviscous Navier–Stokes equation

$$\partial_t \mathbf{u} + \mathbf{u} \cdot \nabla \mathbf{u} = -\nabla p + (-1)^{h+1} \nu_h \nabla^{2h} \mathbf{u} + \mathbf{f}, \quad (1)$$

where ν_h is the specified constant hyperviscosity coefficient, and \mathbf{f} is the forcing function which is described below. Clearly, the ordinary Navier–Stokes equation corresponds to $h=1$ and $\mathbf{f}=0$. We consider the case of periodic boundary conditions

$$\mathbf{u}(\mathbf{x} + \mathcal{L} \hat{\mathbf{e}}_\alpha, t) = \mathbf{u}(\mathbf{x}, t), \quad (\alpha = 1, 2, 3), \quad (2)$$

where \mathcal{L} is the periodicity length and $\hat{\mathbf{e}}_\alpha$ is the unit vector of the α th (Cartesian) coordinate direction. Thus, our solution domain is $\mathcal{B} = [0, \mathcal{L}]^3$. As is well known, because of (2), it is permissible to write $\mathbf{u}(\mathbf{x}, t)$ as a Fourier series

$$\mathbf{u}(\mathbf{x}, t) = \sum_{\boldsymbol{\kappa}} \hat{\mathbf{u}}_{\boldsymbol{\kappa}}(t) e^{i\boldsymbol{\kappa} \cdot \mathbf{x}}, \quad (3)$$

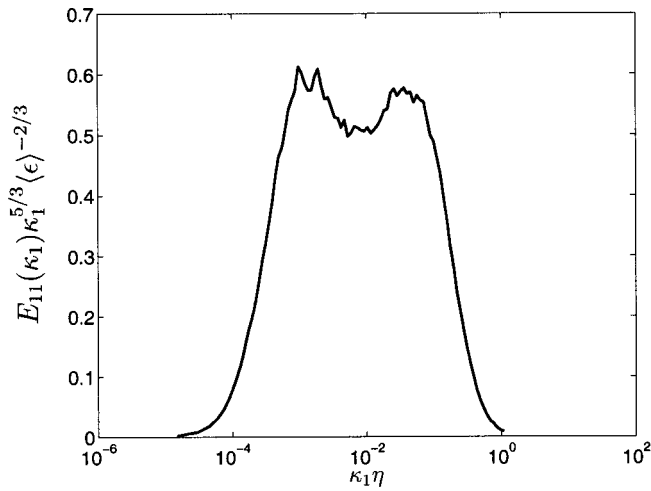


FIG. 1. Compensated longitudinal energy spectrum in homogeneous shear flow at $R_\lambda=915$ [Fig. 5(b) in Shen and Warhaft (2000)].

$$\hat{\mathbf{u}}_\kappa(t) = \frac{1}{\mathcal{L}^3} \int_B \mathbf{u}(\mathbf{x}, t) e^{-i\kappa \cdot \mathbf{x}} d\mathbf{x}, \quad (4)$$

where $\boldsymbol{\kappa} = \kappa_0 \mathbf{n}$ (with $\mathbf{n} \in \mathbb{Z}^3$) and $\kappa_0 = 2\pi/\mathcal{L}$. The Fourier coefficient of $\mathbf{u}(\mathbf{x}, t)$ associated with $\boldsymbol{\kappa}$ is denoted by $\hat{\mathbf{u}}_\kappa(t)$. (Fourier coefficients are denoted by hats.)

Because of homogeneity, the hyperviscous dissipation rate $\langle \epsilon \rangle = (-1)^h \nu_h \langle \mathbf{u} \cdot \nabla^{2h} \mathbf{u} \rangle$ (where angled brackets denote expectation values) may be rewritten as $\nu_h \langle (\nabla^h \mathbf{u})^2 \rangle$, which is a positive semidefinite quantity. (Here ∇^h denotes the outer product of ∇ with itself h times and the square denotes contraction on all indices.) The hyperviscous dissipation wave number is defined by

$$\kappa_d = \left(\frac{\langle \epsilon \rangle}{\nu_h^3} \right)^{1/(6h-2)}. \quad (5)$$

It is easily seen that $\kappa_d = \eta^{-1}$ for $h=1$, where η is the standard Kolmogorov microscale.

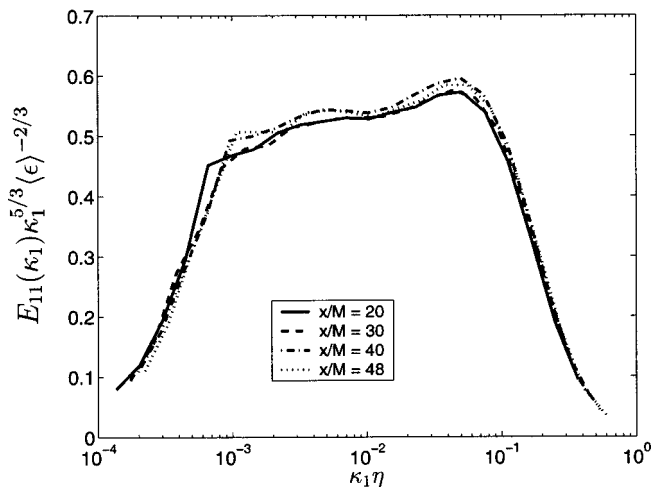


FIG. 2. Compensated longitudinal energy spectra in decaying homogeneous turbulence [processing data presented in Table 2 of Kang *et al.* (2003)] at different stations ($x/M=20, 30, 40, 48$) in the Corrsin wind tunnel (associated Reynolds numbers are $R_\lambda=716, 676, 650, 626$).

In this work, Eq. (1) is driven by an acceleration forcing,¹⁰ so chosen as to yield a constant energy injection rate (denoted by P). The forcing is most simply defined in wave number space by its Fourier coefficients as

$$\hat{\mathbf{f}}_\kappa(t) = \frac{P 1_{[|\kappa| \leq \kappa_f]}}{2k_f(t)} \hat{\mathbf{u}}_\kappa(t), \quad (6)$$

where κ_f is the (specified) largest wavenumber acted upon by the forcing, $1_{[|\kappa| \leq \kappa_f]}$ is the indicator function of the forced shell (unity when $\kappa \leq \kappa_f$, zero otherwise), and k_f is the kinetic energy of the modes within the shell. The forcing drives the flow toward a statistically stationary state wherein

$$\langle \epsilon \rangle = P. \quad (7)$$

Use of \mathbf{f} [as defined by (6)] is unnatural (as are most other ways of forcing turbulence). However, we are primarily concerned with bottleneck effects on energy spectra, i.e., we investigate one particular characteristic of small-scale turbulence. In this case, use of a large-scale forcing^{9,11} (in order to analyze statistically stationary rather than decaying turbulence) is justifiable^{12,13} on the grounds that the details of the forcing have little effect on the small-scale statistics. Indeed, at sufficiently high Reynolds numbers, according to the first Kolmogorov (1941) hypothesis, the small-scale statistics depend on the forcing solely through its energy injection rate.

The Fourier transform of Eq. (1) may be rewritten in the form

$$\begin{aligned} (\hat{\mathbf{u}}_\kappa)_{,t} + \nu_h |\boldsymbol{\kappa}|^{2h} \hat{\mathbf{u}}_\kappa - \frac{P 1_{[|\kappa| \leq \kappa_f]}}{2k_f(t)} \hat{\mathbf{u}}_\kappa(t) \\ = F^{-1}(F \hat{\mathbf{u}}_\kappa)_{,t} = \left[\hat{N}_\kappa - \frac{(\hat{N}_\kappa \cdot \boldsymbol{\kappa}) \boldsymbol{\kappa}}{\kappa^2} \right], \end{aligned} \quad (8)$$

where \hat{N}_κ is the Fourier coefficient of \mathbf{N} ($N_i = -\partial_j u_i u_j$) and

$$F(\boldsymbol{\kappa}, t) = \exp \left\{ \int_0^t \left[(P \kappa_d^2)^{1/3} \left(\frac{|\boldsymbol{\kappa}|}{\kappa_d} \right)^{2h} - \frac{P 1_{[|\kappa| \leq \kappa_f]}}{2k_f(t')} \right] dt' \right\}. \quad (9)$$

In this expression, the hyperviscosity has been rewritten in terms of κ_d using (7) in addition to (5). This simplifies the numerical evaluation of the integrating factor $F(\boldsymbol{\kappa}, t)$ at any t .

III. NUMERICAL METHOD

Equation (9) summarizes the details of our numerical setup. If the flow domain were unbounded, two-dimensional quantities might be set arbitrarily, e.g., P and κ_f , and then the additional specification of κ_d/κ_f would completely characterize the flow. Since our spatial discretization enforces the box size to be the largest lengthscale in the problem, the ratio κ_f/κ_0 also needs to be specified. In our setup, we (arbitrarily) set $P=1$, $\kappa_0=1$; we specify the fixed value $\kappa_f/\kappa_0=3$; then the flow is defined by a single (nondimensional) parameter (e.g., κ_d/κ_f or a suitably defined Reynolds number). Clearly, ℓ

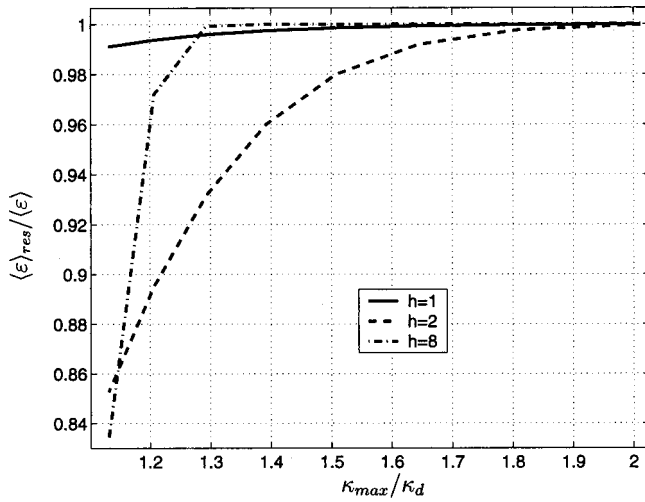


FIG. 3. Resolved fraction of dissipation in model calculations with the 2/9-truncation. The bottleneck and the appropriate rate of decay of $E(\kappa; h)$ in the dissipation range are taken into account in the construction of this figure.

$\equiv \kappa_f^{-1}$, and $\mathcal{U} \equiv (P/\kappa_f)^{1/3}$ are characteristic length and velocity scales of the energy containing motions: thus, a turbulence Reynolds number may be defined as

$$Re = \ell^{2h-1} \mathcal{U} / \nu_h = (\kappa_d / \kappa_f)^{2h-2/3}. \quad (10)$$

Our spatial discretization is pseudo-spectral with N modes in each coordinate direction, and with exact removal of double- and triple-aliasing errors.¹⁴ We investigate small-scale resolution in Fig. 3, that shows the fraction of resolved dissipation for a velocity field generated in the Fourier space according to Eqs. (11) and (16) [with f_η given by Eq. (18)] and truncated according to $|\mathbf{k}| \leq \kappa_{\text{max}}$ (where $\kappa_{\text{max}}/\kappa_0 = \sqrt{2/9}N$). For all values of h , we employ the same “criterion” for accurate small-scale resolution ($\kappa_{\text{max}} \geq 3/2\kappa_d$) that is commonly used in conventional ($h=1$) turbulence simulations.¹¹ Figure 3 shows that, based on this criterion, no less than 99% of $\langle \varepsilon \rangle$ is resolved for $h=1$ and 8, and 98% for $h=2$. The small-scale resolution criterion may be rewritten as $N \geq 3\sqrt{9/8}\kappa_d/\kappa_0$. This guarantees that, for the range of resolutions $N \in [160, 300]$ considered in this work, the remaining (single-)aliasing error energy is always less than 0.01% of the resolved kinetic energy. Figures 4 and 5 show the effect of grid and time-step refinement on the compensated energy spectrum for a flow with $h=1$, $\kappa_d/\kappa_0=50$. Figure 5 suggests that (peak) relative errors never exceed 11.1%.

The initial field is a random realization¹⁵ of a vector field with prescribed energy spectrum, i.e.,

$$\hat{u}_\kappa(0) = \sqrt{\frac{E(\kappa, 0)}{2\pi\kappa^2}} [\cos \varphi e^{i\theta_1} \hat{\xi}_1 + \sin \varphi e^{i\theta_2} \hat{\xi}_2]. \quad (11)$$

Here θ_1 , θ_2 are the phases of \hat{u}_1 and \hat{u}_2 , respectively, 1, 2 being directions (whose unit vectors are denoted by $\hat{\xi}_{1,2}$) in the incompressibility plane ($\mathbf{k} \cdot \hat{u}_\kappa = 0$) corresponding to the Euler angles in the x (or y) convention.¹⁶ The azimuth of the vector $(|\hat{u}_1|, |\hat{u}_2|)$ (in that plane) is equal to φ . We follow

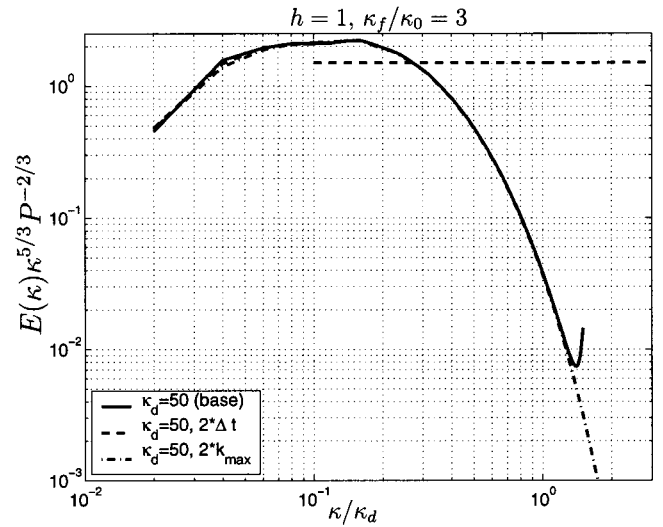


FIG. 4. Compensated energy spectra for $\kappa_d/\kappa_0=50$ (with $h=1$ and $\kappa_f/\kappa_0=3$; thicker horizontal dashed line at 1.5). “Base” refers to $\Delta t=10^{-3}$ and $N=160$, whereas “2Δt” and “2κ_{max}” refer to the same case advanced with $\Delta t=2 \times 10^{-3}$, $N=160$ and $\Delta t=10^{-3}$, $N=320$, respectively.

Rogallo¹⁵ and choose θ_1 , θ_2 , $\varphi \in \mathcal{U}([0, 2\pi])$ (uniform random deviates in $[0, 2\pi]$) subject to the requirement of Hermitian symmetry for the Fourier coefficients. We choose the initial energy spectrum to be

$$E(\kappa, 0) = \frac{9}{11} u_0'^2 \kappa_f^{-1} \times \begin{cases} (\kappa/\kappa_f)^2, & \kappa \leq \kappa_f, \\ (\kappa/\kappa_f)^{-5/3}, & \kappa > \kappa_f, \end{cases} \quad (12)$$

where u_0' denotes the initial root-mean square-intensity of any one velocity component (we set $u_0'=1$).

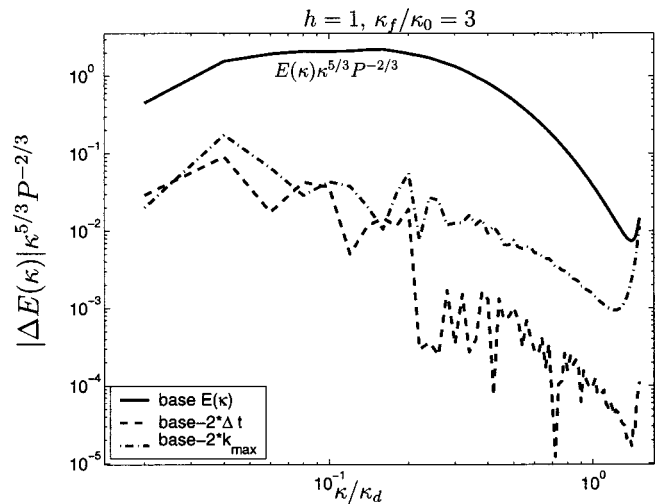


FIG. 5. Absolute error (dashed, dot-dashed) in steady-state compensated energy spectra between the “base” and “2Δt” simulations, and between the “base” and “2κ_{max}” simulations. The spectral turn-up in the “base” $E(\kappa)$ (solid) in a left neighborhood of κ_{max} is the result of single-aliasing errors. This makes the difference compensated spectrum between the “base” and “2κ_{max}” simulations meaningless in a left neighborhood of κ_{max} .

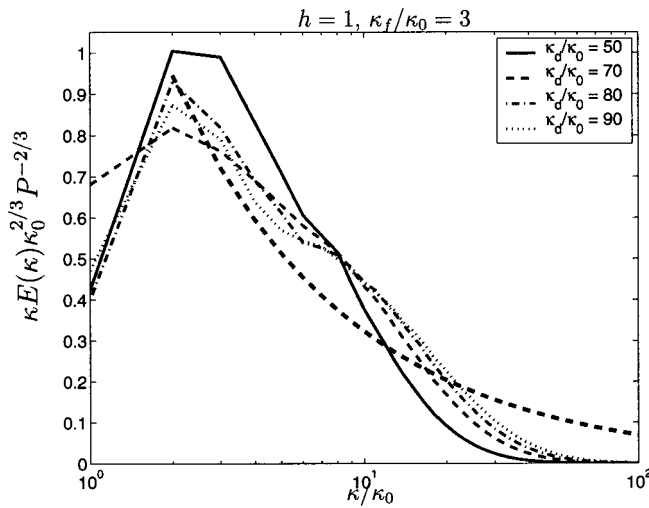


FIG. 6. Energy spectra for different values of κ_d/κ_0 with $h=1$ and $\kappa_f/\kappa_0=3$. The thicker dashed line is the Kolmogorov spectrum, Eq. (14).

We use a second-order Runge–Kutta for time advancement. In a series of tests, we checked that statistical stationarity may be assumed after 10–15 eddy turnover times (the number of eddy turn-over times that the flow has undergone at time t is defined as $\tau_e=(P\kappa_f^2)^{1/3}t$).

Whenever isotropy is postulated in (a discrete) wave number space, a discretization in wave number shells of thickness κ_0 is implied for the energy spectrum. This function is computed as

$$E(n\kappa_0) = \frac{1}{M'(n\kappa_0)} \sum_{(n-1/2)\kappa_0 \leq |\mathbf{k}| < (n+1/2)\kappa_0} \frac{|\hat{\mathbf{u}}_{\mathbf{k}}|^2}{2}, \quad (13)$$

where $n=1, 2, \dots, N/2$ and $M'(n\kappa_0)=M(n\kappa_0)/\{(4\pi/3)[(n+1/2)^3-(n-1/2)^3]\}$, $M(n\kappa_0)$ being the number of modes contained in the shell centered at $n\kappa_0$ [as indicated in the sum in (13)].¹⁷ In subsequent figures, we show time-averaged energy spectra, with the time-averaging starting at $\tau_e=10$.

IV. RESULTS

Figure 6 shows energy spectra for $h=1$ and different values of κ_d/κ_0 . Associated Reynolds numbers [using Eq. (10)] are in the range [43, 93], whereas $N \in [160, 300]$. Taylor Reynolds numbers ($R_\lambda = \sqrt{20k^2/(3\nu\epsilon)}$) = $k\sqrt{20/3}/(\nu\kappa_d)^2$) are indicated in Table I. The unsteadiness in the time series for the turbulence kinetic energy (denoted by k , or TKE), as defined by a volume average of $|\mathbf{u}|^2/2$, requires the additional use of time-averaging to finally infer the values of R_λ reported in Table I.

TABLE I. Parameters for DNS with $h=1$.

κ_d/κ_0	N	ν	Re	R_λ
50	160	5.428×10^{-3}	43	84
70	240	3.466×10^{-3}	67	105
80	256	2.900×10^{-3}	80	112
90	300	2.479×10^{-3}	93	128

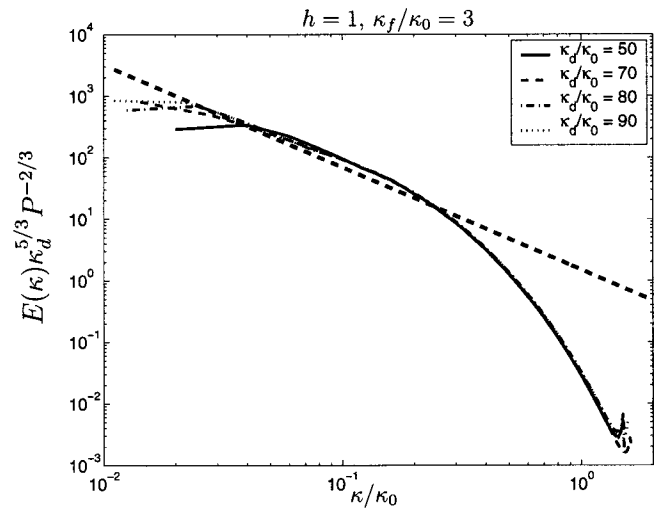


FIG. 7. Kolmogorov-scaled energy spectra for different values of κ_d/κ_0 with $h=1$ and $\kappa_f/\kappa_0=3$. The thicker dashed line is the Kolmogorov spectrum, Eq. (14).

Figure 7 shows Kolmogorov-scaled energy spectra compared to the Kolmogorov inertial-range spectrum

$$\hat{E}(\kappa/\kappa_d) = C(\kappa/\kappa_d)^{-5/3}, \quad (14)$$

with $C=1.5$. As may be seen, at the higher wave numbers ($\kappa/\kappa_d > 0.1$) there is an excellent collapse of the spectra for different values of κ_d/κ_0 indicating that Kolmogorov scaling is satisfied to good accuracy. In Fig. 8, compensated spectra are consistent with the observation⁵ that the correct plateau to look at to infer the value of the Kolmogorov constant is to the left of what can be described as a bottleneck peak. Recent numerical simulations^{5–7} show that a true inertial-range plateau in the compensated spectra may be clearly visible for Reynolds numbers R_λ larger than (at least) 200 (requiring a minimum of 512^3 modes). From Fig. 8, we see that the bottleneck bump starts in proximity of $\kappa/\kappa_d=0.05$. This is in

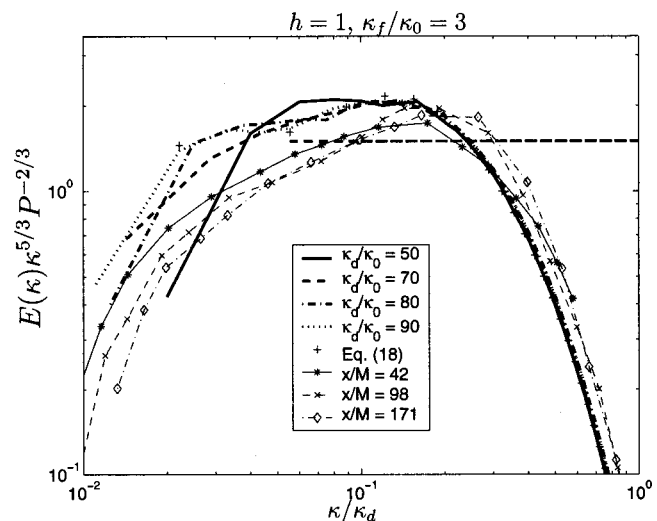


FIG. 8. Compensated energy spectra for different values of κ_d/κ_0 with $h=1$ and $\kappa_f/\kappa_0=3$ (thicker dashed line at 1.5). Eq. (18) (+ marks) and the Comte-Bellot and Corrsin (Ref. 24) experimental data (thin lines with *, x and diamond marks) are also indicated.

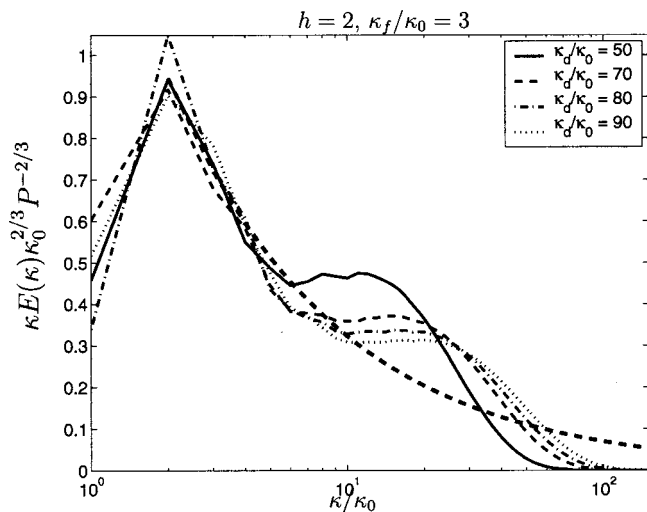


FIG. 9. Energy spectra for different values of κ_d/κ_0 with $h=2$ and $\kappa_f/\kappa_0=3$. The thicker dashed line is the Kolmogorov spectrum, Eq. (14).

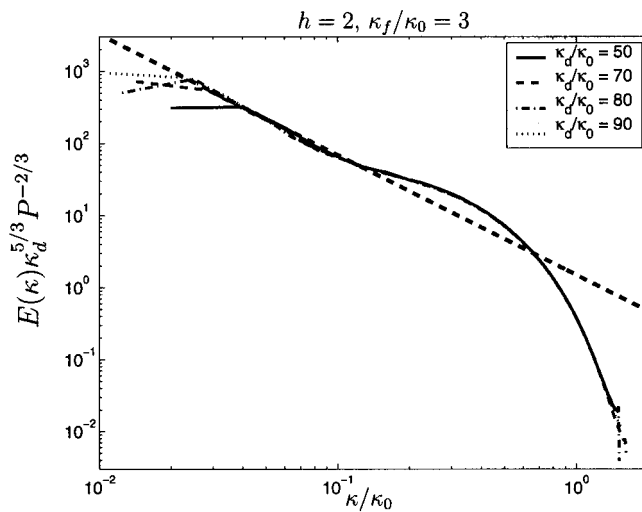


FIG. 10. Kolmogorov-scaled energy spectra for different values of κ_d/κ_0 with $h=2$ and $\kappa_f/\kappa_0=3$. The thicker dashed line is the Kolmogorov spectrum, Eq. (14).

good accord with higher resolution data.⁶ Thus, the necessary condition for a value for the Kolmogorov constant to be discernible from the compensated spectra is the presence of a plateau for $\kappa/\kappa_d < 0.05$ (a clear inertial-range plateau is missing from Fig. 8).

Two comments are in order. First, much scatter in values for the Kolmogorov constant (based on various experimental and numerical investigations^{18,19}) might be probably reduced by distinguishing between analyses that recognize the existence of a bottleneck and those that do not (see, e.g., Fig. 1 of Ref. 19). Second, bottleneck effects are not incompatible with the conventional Richardson–Kolmogorov phenomenology of turbulence [as it is easy to see by interrogating the Kolmogorov (1941) hypotheses] and they are manifest not only at moderately high Reynolds numbers²⁰ that may be simulated on 512³ (or larger) grids but also at lower Reynolds numbers where no scaling arguments may be invoked. Bottleneck effects are the result of viscous effects on inertial transfer.

Figures 9–14 show analogous data for $h=2$ and $h=8$. From the compensated spectra, it may be seen that the bottleneck peak increases as h increases (for all ν_h), whereas its location shifts to larger κ/κ_d . This is summarized in Fig. 16.

A. Modeling of numerical spectra

A fundamental consequence of the Kolmogorov (1941) hypotheses is that the energy spectrum in the universal equilibrium range^{21,22} of an isotropic, forced turbulence is given by

$$E(\kappa) = CP^{2/3} \kappa^{-5/3} f_\eta(\kappa/\kappa_d). \tag{15}$$

A model spectrum which is a natural extension of this relation to arbitrary κ

$$E_m(\kappa) = f_L(\kappa/\kappa_f) CP^{2/3} \kappa^{-5/3} f_\eta(\kappa/\kappa_d), \tag{16}$$

was proposed by Pope.²² Clearly, f_L represents the spectrum behavior in the infrared and energy containing ranges, and f_η represents the dissipation range behavior. For large κ/κ_f ,

$f_L(\kappa/\kappa_f)$ tends to unity, as does $f_\eta(\kappa/\kappa_d)$ for small κ/κ_d . Thus, for $\kappa_f \ll \kappa \ll \kappa_d$, the model spectrum is a Kolmogorov $-5/3$ -spectrum with constant C . While f_L is not universal (having a first-order dependence on the large scales of the flow), according to the Kolmogorov hypotheses, f_η is universal (for given h).

Use of (16) with modeled forms for f_L and f_η constitutes an empirical model for the energy spectrum. This is useful in experimental investigations,^{4,23} where $E(\kappa)$ has to be deduced from experimental data for $E_{11}(\kappa_1)$. We also suggest that a model spectrum (that reproduces the important physical observations) may be used as a predictive tool to investigate turbulence statistics in the infinite Reynolds number limit (as shown further below).

The capability of Pope’s model spectrum to account for

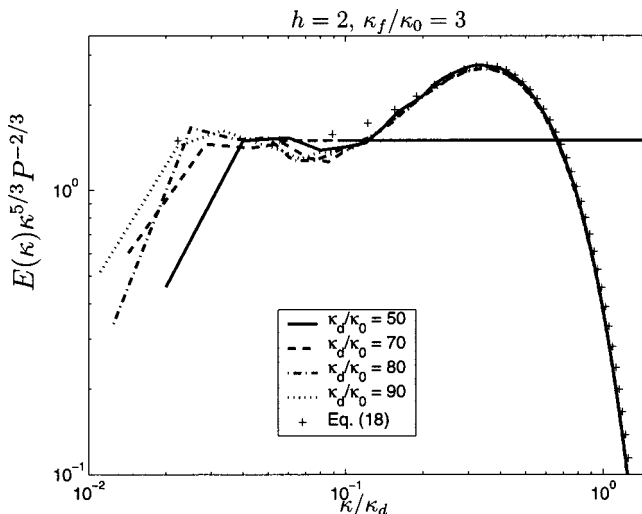


FIG. 11. Compensated energy spectra for different values of κ_d/κ_0 with $h=2$ and $\kappa_f/\kappa_0=3$ (thicker straight line is at 1.5). Equation (18) (+ marks) is also indicated.

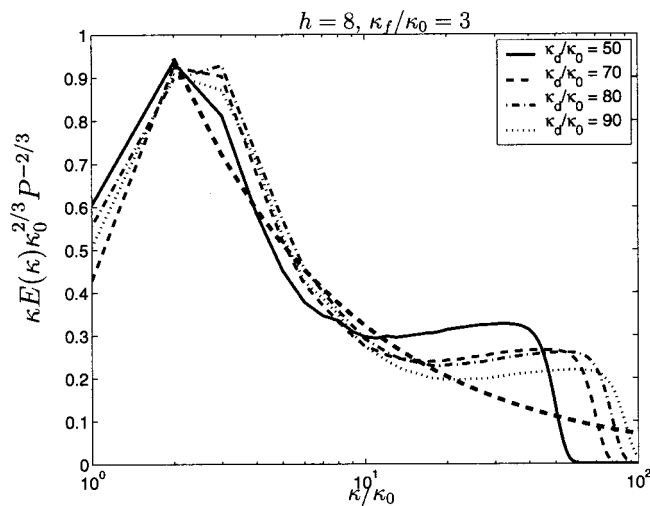


FIG. 12. Energy spectra for different values of κ_d/κ_0 with $h=8$ and $\kappa_f/\kappa_0=3$. The thicker dashed line is the Kolmogorov spectrum, Eq. (14).

a bottleneck depends on the form chosen for the dissipation range component f_η . A recent proposal²³ (for $h=1$) is the result of empirical modeling

$$f_\eta(x) = \left[1 + \alpha_5 \left(\frac{1}{\pi} \arctan\{\alpha_6 \log_{10} x + \alpha_7\} + \frac{1}{2} \right) \right] \times \exp(-\alpha_4 x), \tag{17}$$

where the α_i 's are determined by comparing with measurements (x being a dummy variable).

Following a similar approach, we are able to match the dissipation range components of our data to good accuracy (see Figs. 15 and 16) through

$$f_\eta(x) = \left\{ 1 + \frac{A}{2} \{ 1 + \text{erf}[(1.1 + 0.3\sigma x) \ln(\sigma x)] \} \right\} \times \exp(-bx^h), \tag{18}$$

where A and σ are determined by an interpolation procedure

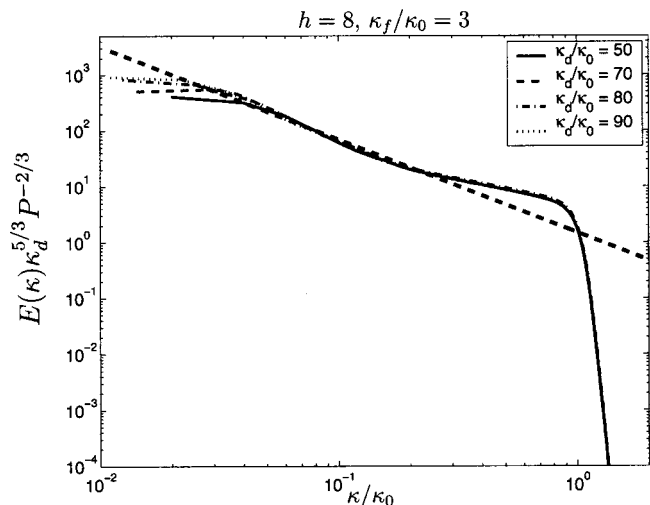


FIG. 13. Kolmogorov-scaled energy spectra for different values of κ_d/κ_0 with $h=8$ and $\kappa_f/\kappa_0=3$. The thicker dashed line is the Kolmogorov spectrum, Eq. (14).

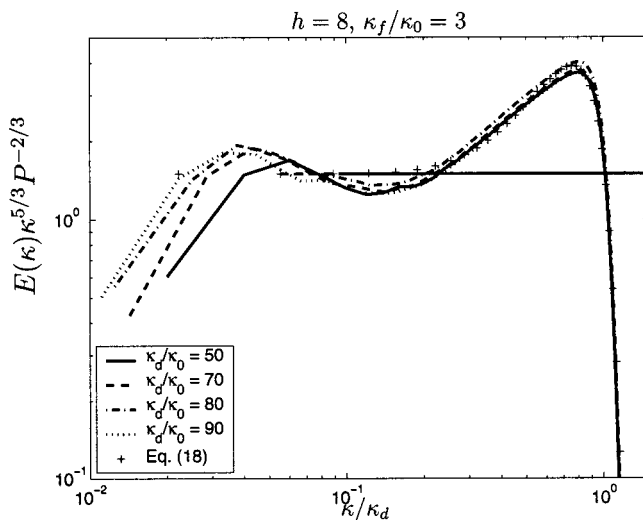


FIG. 14. Compensated energy spectra for different values of κ_d/κ_0 with $h=8$ and $\kappa_f/\kappa_0=3$ (thicker straight line is at 1.5). Equation (18) (+ marks) is also indicated.

for each value of h (given κ_d/κ_0). Tables II and III give the values of A and σ for each of our calculations; based on these data, one may hypothesize (as we do hereafter) that A , σ are “independent” of κ_d/κ_0 (at least over the range of values considered here).

Examination of the numerical compensated spectra shows the exponential component of f_η to be of the form $\exp(a_1 - b_1 x^h)$. However, when the factor preceding the exponential is modeled as in Eq. (18), we can no longer guarantee that Eq. (18) with $b=b_1$ satisfies

$$\frac{1}{2C} = \int_0^\infty x^{2h-5/3} f_L(x \kappa_d/\kappa_f) f_\eta(x) dx. \tag{19}$$

This condition is equivalent to

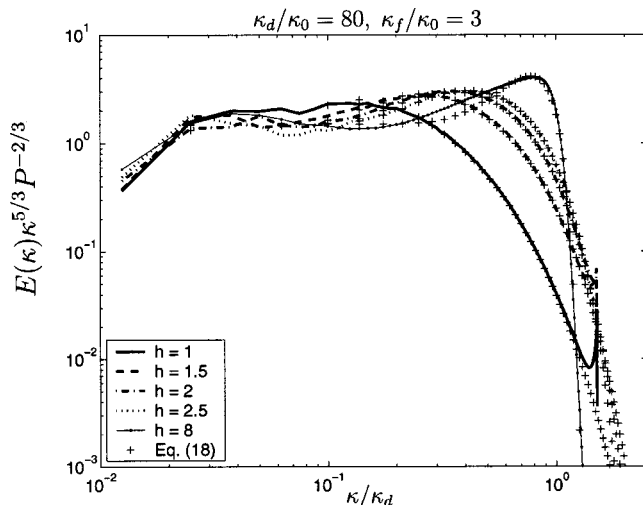


FIG. 15. Compensated energy spectra for different values of h and $\kappa_d/\kappa_0=80$ (with $\kappa_f/\kappa_0=3$) vs corresponding model curves computed through Eq. (18) (+ marks).

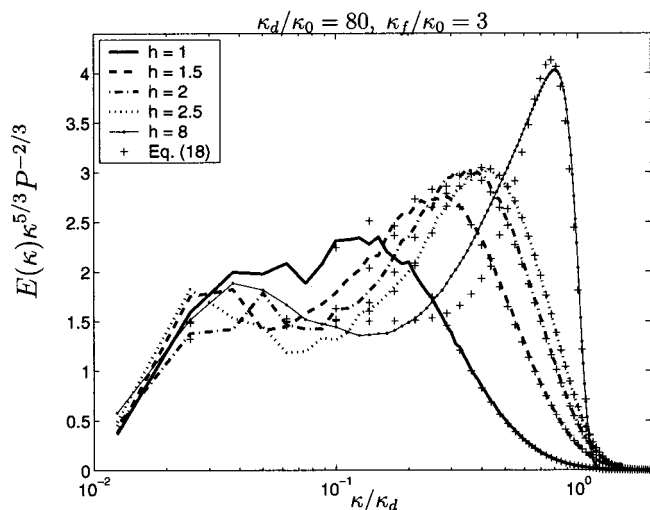


FIG. 16. Compensated energy spectra for different values of h and $\kappa_d/\kappa_0 = 80$ (with $\kappa_f/\kappa_0=3$) vs corresponding model curves computed through Eq. (18) (+ marks).

$$P = \langle \varepsilon \rangle = 2\nu_h \int_0^\infty \kappa^{2h} E(\kappa) d\kappa, \quad (20)$$

applied to the model spectrum, Eq. (16). For given f_L , Eq. (19) imposes a condition on f_η . Having determined the dependences of A and σ on h , we solve (19) for b (using a secant method). The resulting values are given in Table IV for $\kappa_d/\kappa_0=90$.

Figures 17 and 18 show that matching of numerical spectra in the dissipation range through Eq. (17) [as opposed to Eq. (18)] is also possible, after trial and error tuning of the α_i 's to values different from those indicated by Kang *et al.*⁴

The procedure above has been described under the assumption that the functional form for f_L is known. We now describe the rationale to obtain the form actually used in this work. Our goal is to determine an approximate expression to describe the large-scale behavior of the energy spectrum in such a special (homogeneous) turbulence as the one driven by the forcing defined by (6). In contrast to the case of f_η there is no suggestion that f_L is universal.

Having decided that f_η is given by Eq. (18), an empirically determined f_L [defined as $f_L^{(e)} = E(\kappa)/(CP^{2/3}\kappa^{-5/3}f_\eta)$] may be computed as soon as the energy spectrum from one numerical simulation is known. Empirically determined f_L 's were computed for different realizations of different flows (corresponding to different values of h and κ_d/κ_0). For each flow, we compared eight independent realizations of $f_L^{(e)}$ with their ensemble average and the following model expression:

TABLE II. Values of A based on different κ_d/κ_0 .

κ_d/κ_0	$h=1$	$h=2$	$h=8$
50	2.9277	2.3198	4.6240
70	3.5151	1.9312	4.5722
80	3.1849	2.1297	4.5863
90	2.9574	2.1071	4.2530

TABLE III. Values of σ based on different κ_d/κ_0 .

κ_d/κ_0	$h=1$	$h=2$	$h=8$
50	11.83	4.220	1.266
70	10.03	3.815	1.268
80	9.536	3.927	1.266
90	10.71	3.907	1.262

$$f_L(x) = \left[\frac{ax + \exp(cx^q) - 1}{\exp(cx^q)} \right]^{5/3+p}, \quad (21)$$

with $a=1.6$, $c=3.5$, $q=1.5$, and $p=2$. As expected, we found (i) the empirically determined f_L 's (for each flow) to be strongly realization-dependent, (ii) their ensemble average to be flow-dependent.

Therefore, we elect to model f_L once and for all as in Eq. (21). The resulting model spectrum is capable of matching numerical energy spectra to good accuracy (reasonable accuracy may be achieved at the large scales, with relative errors $|(E(\kappa) - E_m(\kappa))/E_m(\kappa)|$ never exceeding 0.4). Representative results are those in Figs. 19 and 20.

B. Asymptotic behavior of model TKE

In this section, we consider a model kinetic energy difference ratio (i.e., defined in terms of the model spectrum) in an asymptotic regime as the Reynolds number grows unbounded. In this case, the effect of large-scale motions (this includes the details of the modeling for f_L) vanishes as $Re \rightarrow \infty$.

Figures 6, 9, and 12 suggest that as κ_d/κ_0 is increased, there are two competing effects determining the TKE behavior with Reynolds number. As Re grows, the energy spectra extend to higher and higher wave numbers, with an attendant increase in the TKE. On the other hand, a less intense bottleneck is required for the dissipation rate to balance the energy flux through the inertial range as this is stretched to higher wave numbers. The two effects may be clearly seen in Figs. 9 and 12.

For given fixed values of P , κ_0 , h , and κ_f , we denote by $E_m(\kappa; \kappa_d)$ the model energy spectrum which depends on the specified value of κ_d . The corresponding kinetic energy is

$$k(\kappa_d) \equiv \int_0^\infty E_m(\kappa; \kappa_d) d\kappa. \quad (22)$$

We are particularly interested in the behavior of $k(\kappa_d)$ as κ_d tends to infinity, and so define $k_\infty = k(\infty)$ and $\Delta k(\kappa_d) = k(\kappa_d) - k_\infty$. It follows from the model [Eq. (16)] that

TABLE IV. Values of model coefficients for $\kappa_d/\kappa_0=90$.

	$h=1$	$h=2$	$h=8$
A	2.9574	2.1071	4.2530
σ	10.71	3.907	1.262
b	4.996	2.315	1.239

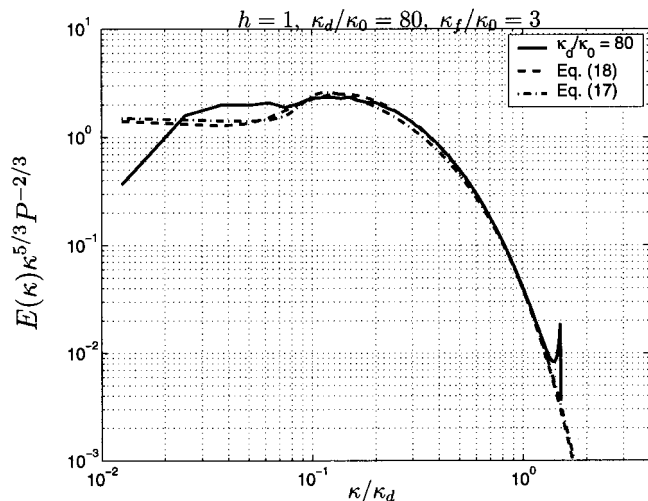


FIG. 17. Compensated energy spectrum (solid) for $h=1$ and $\kappa_d/\kappa_0=80$ (with $\kappa_f/\kappa_0=3$) compared with Eq. (18) (dashed) and Eq. (17) (dot-dashed). Values of α_i yielding reasonable agreement between the predictions of Eqs. (18) and (17) are $\alpha_4=4.9$, $\alpha_5=2.55$, $\alpha_6=15$, $\alpha_7=15.5$.

$$\frac{\Delta k(\kappa_d)}{k_\infty} = \left(\frac{\kappa_d}{\kappa_f}\right)^{-2/3} \frac{\int_0^\infty f_L(y\kappa_d/\kappa_f)y^{-5/3}[f_\eta(y)-1]dy}{\int_0^\infty f_L(x)x^{-5/3}dx}. \quad (23)$$

It is evident that for asymptotically large κ_d/κ_f

$$\Delta k/k_\infty \approx \left(\frac{\kappa_d}{\kappa_f}\right)^{-2/3} D(h). \quad (24)$$

This is a consequence of the first Kolmogorov (1941) hypothesis (independent of the particular representation used for E_m). Because of Eq. (16), the asymptotic slope in Eq. (24) takes the form

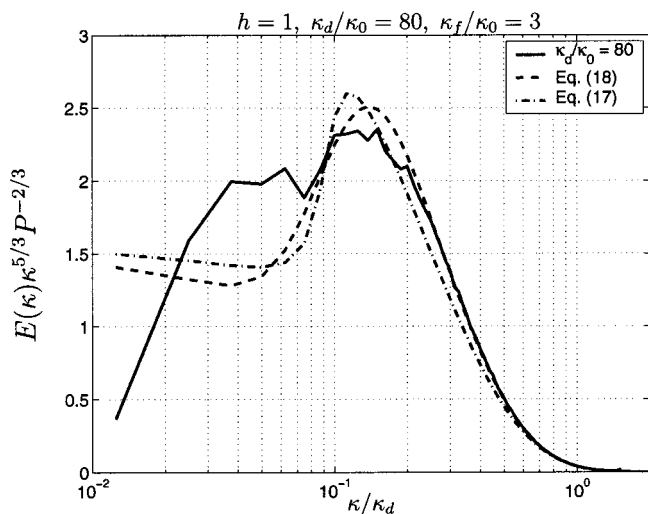


FIG. 18. Compensated energy spectrum (solid) for $h=1$ and $\kappa_d/\kappa_0=80$ (with $\kappa_f/\kappa_0=3$) compared with Eq. (18) (dashed) and Eq. (17) (dot-dashed). Values of α_i yielding reasonable agreement between the predictions of Eqs. (18) and (17) are $\alpha_4=4.9$, $\alpha_5=2.55$, $\alpha_6=15$, $\alpha_7=15.5$.

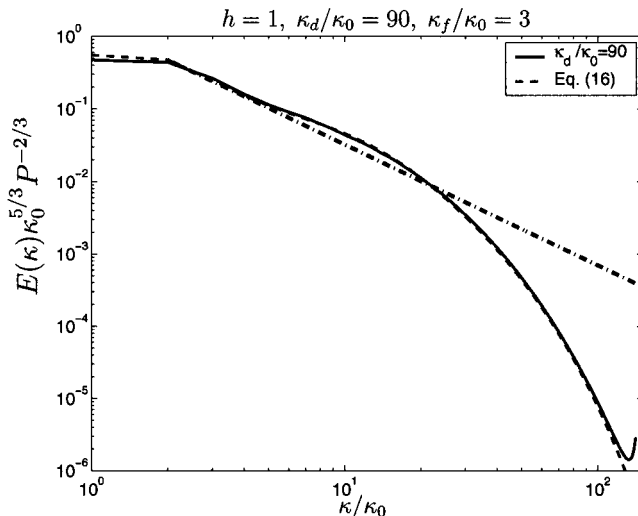


FIG. 19. Numerical energy spectrum (solid) for $h=1$ and $\kappa_d/\kappa_0=90$ (with $\kappa_f/\kappa_0=3$) vs model spectrum Eq. (16) (dashed). The dot-dashed line is the Kolmogorov spectrum, Eq. (14).

$$D(h) = \frac{\int_0^\infty y^{-5/3}[f_\eta(y)-1]dy}{\int_0^\infty f_L(x)x^{-5/3}dx}. \quad (25)$$

Values for $D(h)$ corresponding to Eq. (18) are given in Table V. As may be seen, for $h=2$ and 8 , $D(h)$ is positive, indicating that $k(\kappa_d)$ decreases as κ_d/κ_f increases: The positive contribution from the longer tail is outweighed by the decreased contribution from the reduced bump. For $h=1$, the value of $D(h)$ is negative, suggesting to opposite behavior, but this result needs qualification, which is now given.

It is easily seen that the behavior of the integrand in the numerator on the right-hand side of (23) is nonphysical as $y \rightarrow 0$. This is particularly true for $h=1$ (see Fig. 21). In this case, the integrand in the numerator on the right-hand side of (25) has a singularity at the origin of the form $-by^{-2/3}$. Even though this singularity is integrable, it yields a nonphysical negative contribution to $D(1)$ [negative values for $D(h)$ are

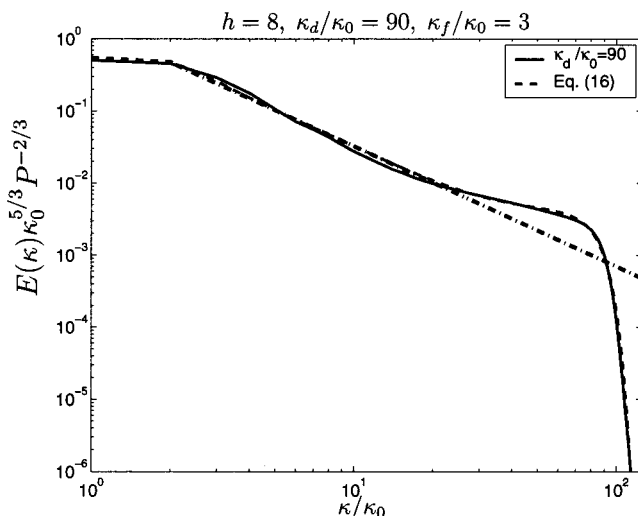


FIG. 20. Numerical energy spectrum (solid) for $h=8$ and $\kappa_d/\kappa_0=90$ (with $\kappa_f/\kappa_0=3$) vs model spectrum Eq. (16) (dashed). The dot-dashed line is the Kolmogorov spectrum, Eq. (14).

TABLE V. Values of $D(h)$ for $h=1, 2, 8$.

	$h=1$	$h=2$	$h=8$
$D(h)$	-1.262	0.2855	0.0734

not ruled out unless they result from unphysical effects in the modeling]. The values for $D(2)$, $D(8)$ in Table V are reasonable as there is no singularity for $h > 5/3$.

We conclude that an improved model for f_η is required to correctly represent the nondimensional kinetic energy difference spectra [appearing in the integrand in the numerator of (23)] for small values of y . Computation of the asymptotic slope $D(h)$ requires that an improved representation of such spectra be available in an asymptotic regime as $\kappa_d/\kappa_f \rightarrow \infty$.

V. CONCLUSIONS

Accurate numerical simulations have been performed of forced homogeneous isotropic turbulence evolving according to the hyperviscous Navier–Stokes equation. Values of the hyperviscosity index h between 1 (corresponding to ordinary Navier–Stokes) and 8 are considered. Using N^3 Fourier modes (with N up to 300) simulations are performed with length-scale ratios κ_d/κ_0 up to 90. For $h=1$, the largest Taylor-scale Reynolds number achieved is 128.

In all cases, the high-wave number spectra are found to be self-similar under Kolmogorov scaling. In the dissipation range, the spectra decay as $\exp(-b(\kappa/\kappa_d)^h)$.

As summarized in Fig. 16, the compensated spectra reveal a spectral bump. The value of the peak of the bump increases with h (from about 2.3 for $h=1$ to approximately 4 for $h=8$) and it moves to higher wave number (from $\kappa/\kappa_d \approx 0.15$ for $h=1$ to $\kappa/\kappa_d \approx 0.8$ for $h=8$).

The spectra from the simulations are well represented by the model spectrum, Eq. (16), with the empirical expression Eq. (18) for the dissipation range function f_η .

As κ_d/κ_f increases, the spectrum extends to higher wave numbers (tending to increase the TKE), but the energy asso-

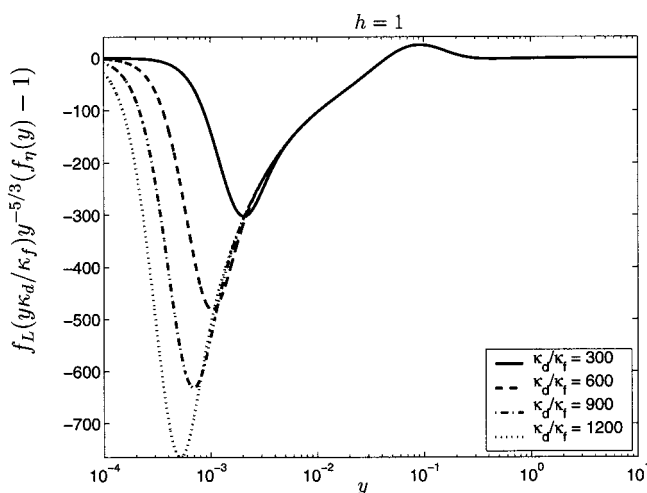


FIG. 21. Model kinetic energy difference spectra for $h=1$ and different values of κ_d/κ_f [computed on the basis of Eqs. (16), (18), and (21)].

ciated with the bump decreases. The net effect (as predicted by the first Kolmogorov hypothesis) is that the TKE behaves as $\Delta k/k_\infty \approx D(h)(\kappa_d/\kappa_f)^{-2/3}$ as $\kappa_d/\kappa_f \rightarrow \infty$.

The model spectrum [as given by Eqs. (16), (18), and (21)] is found to be inadequate to estimate the asymptotic slope $D(1)$. Reasonable values are obtained for $D(h)$ with $h=2, 8$.

ACKNOWLEDGMENTS

This work was supported in part by NSF Grant No. CTS-0328329, with computational resources provided by the Cornell Theory Center (CTC). We are grateful to Steve Lantz, John Zollweg, and Daniel Sverdluk of the CTC for assistance to run on the Velocity cluster. Helpful discussions with Professor P. K. Yeung and Professor L. R. Collins are gratefully acknowledged.

- ¹S. G. Saddoughi and S. V. Veeravalli, "Local isotropy in turbulent boundary layers at high Reynolds number," *J. Fluid Mech.* **268**, 333 (1994).
- ²S. G. Saddoughi, "Local isotropy in turbulent boundary layers at high Reynolds number," *J. Fluid Mech.* **348**, 201 (1997).
- ³X. Shen and Z. Warhaft, "The anisotropy of the small scale structure in high Reynolds number turbulent shear flow," *Phys. Fluids* **12**, 2976 (2000).
- ⁴H. S. Kang, S. Chester, and C. Meneveau, "Decaying turbulence in an active generated grid flow and comparison with large eddy simulation," *J. Fluid Mech.* **480**, 129 (2003).
- ⁵P. K. Yeung and Y. Zhou, "Universality of the Kolmogorov constant in numerical simulations of turbulence," *Phys. Rev. E* **56**, 1746 (1997).
- ⁶T. Gotoh, D. Fukayama, and T. Nakano, "Velocity field statistics in homogeneous steady turbulence obtained using a high resolution DNS," *Phys. Fluids* **14**, 1065 (2002).
- ⁷Y. Kaneda, T. Ishihara, M. Yokokawa, K. Itakura, and A. Uno, "Energy dissipation rate and energy spectrum in high resolution DNS of turbulence in a periodic box," *Phys. Fluids* **14**, L21 (2003).
- ⁸T. Ishihara and Y. Kaneda, "High resolution DNS of incompressible homogeneous forced turbulence: time dependence of the statistics," in *Statistical Theories and Computational Approaches to Turbulence*, edited by Y. Kaneda and T. Gotoh (Springer, Berlin, 2002), pp. 177–188.
- ⁹V. Borue and S. A. Orszag, "Local energy flux and subgrid-scale statistics in 3D turbulence," *J. Fluid Mech.* **366**, 1 (1998).
- ¹⁰A. A. Wray, private communication (2002).
- ¹¹P. K. Yeung and S. B. Pope, "Lagrangian statistics from direct numerical simulations of isotropic turbulence," *J. Fluid Mech.* **207**, 531 (1989).
- ¹²M. R. Overholt and S. B. Pope, "A deterministic forcing scheme for direct numerical simulations of turbulence," *Comput. Fluids* **27**, 11 (1998).
- ¹³V. Eswaran and S. B. Pope, "An examination of forcing in direct numerical simulations of turbulence," *Comput. Fluids* **16**, 257 (1988).
- ¹⁴G. S. Patterson and S. A. Orszag, "Spectral calculations of isotropic turbulence: Efficient removal of aliasing interactions," *Phys. Fluids* **14**, 2538 (1971).
- ¹⁵R. S. Rogallo, "Numerical experiments in homogeneous turbulence," NASA TM 81315 (1981).
- ¹⁶H. Goldstein, *Classical Mechanics*, 2nd ed. (Addison Wesley, Menlo Park, CA, 1980).
- ¹⁷V. Eswaran and S. B. Pope, "Direct numerical simulations of the turbulent mixing of a passive scalar," *Phys. Fluids* **31**, 506 (1988).
- ¹⁸Y. Zhou and C. G. Speziale, "Advances in the fundamental aspects of turbulence: Energy transfer, interacting scales, and self-preservation of isotropic decay," *Appl. Mech. Rev.* **51**(4), 267 (1998).
- ¹⁹K. R. Sreenivasan, "On the universality of the Kolmogorov constant," *Phys. Fluids* **7**, 2778 (1995).

- ²⁰W. Dobler, N. E. L. Haugen, T. A. Yousef, and A. Brandeburg, "Bottle-neck effect in 3D turbulence simulations," *Phys. Rev. E* **68**, 026304 (2003).
- ²¹G. K. Batchelor, *The Theory of Homogeneous Turbulence* (Cambridge University Press, Cambridge, U.K., 1953).
- ²²S. B. Pope, *Turbulent Flows* (Cambridge University Press, Cambridge, U.K., 2000).
- ²³S. Cerutti and C. Meneveau, "Statistics of filtered velocity in grid and wake turbulence," *Phys. Fluids* **12**, 1143 (2000).
- ²⁴G. Comte-Bellot and S. Corrsin, "Simple Eulerian time correlation of full- and narrow-band velocity signals in grid-generated, isotropic turbulence," *J. Fluid Mech.* **48**, 273 (1971).